LETTERS
https://doi.org/10.1038/s41565-019-0466-2
nature nanotechnology

Strain-based room-temperature non-volatile $MoTe_2$ ferroelectric phase change transistor

Wenhui Hou[1], Ahmad Azizimanesh[1], Arfan Sewaket[1], Tara Peña[1], Carla Watson[2], Ming Liu[3], Hesam Askari[4] and Stephen M. Wu[1,2*]

The primary mechanism of operation of almost all transistors today relies on the electric-field effect in a semiconducting channel to tune its conductivity from the conducting 'on' state to a non-conducting 'off' state. As transistors continue to scale down to increase computational performance, physical limitations from nanoscale field-effect operation begin to cause undesirable current leakage, which is detrimental to the continued advancement of computing[1,2]. Using a fundamentally different mechanism of operation, we show that through nanoscale strain engineering with thin films and ferroelectrics the transition metal dichalcogenide $MoTe_2$ can be reversibly switched with electric-field-induced strain between the 1T′-$MoTe_2$ (semimetallic) phase to a semiconducting $MoTe_2$ phase in a field-effect transistor geometry. This alternative mechanism for transistor switching sidesteps all the static and dynamic power consumption problems in conventional field-effect transistors[3,4]. Using strain, we achieve large non-volatile changes in channel conductivity ($G_{on}/G_{off} \approx 10^7$ versus $G_{on}/G_{off} \approx 0.04$ in the control device) at room temperature. Ferroelectric devices offer the potential to reach sub-nanosecond non-volatile strain switching at the attojoule/bit level[5–7], with immediate applications in ultrafast low-power non-volatile logic and memory[8] while also transforming the landscape of computational architectures because conventional power, speed and volatility considerations for microelectronics may no longer exist.

We designed our device using single-crystal oxide substrates of the relaxor ferroelectric $Pb(Mg_{1/3}Nb_{2/3})_{0.71}Ti_{0.29}O_3$ (PMN-PT) as the gate dielectric (0.25–0.3 mm thickness). On top of this ferroelectric substrate we exfoliated 1T′-$MoTe_2$ (13–70 nm) from a single crystal source, then patterned devices using Ni contact pads (Fig. 1a,b). Exfoliation was performed in a humidity-controlled environment for increased adhesion. Depending on the contact material, stress from the deposited thin film strained the $MoTe_2$ channel at the contact pads, analogous to the uniaxial strain techniques from strained silicon technology, widely adopted in industrial CMOS processes[9]. We found that contact metal stress and transition metal dichalcogenide (TMDC) to substrate adhesion are both critically important for obtaining a functional device. During fabrication we were careful not to increase the temperature of the ferroelectric above 80 °C, well below the ferroelectric's Curie temperature of 135 °C (sudden quenching through the transition causes the size of the domains to shrink from the few micrometres scale to the nanometre scale[10], setting a complicated strain state within the $MoTe_2$; Supplementary Figs. 1 and 2).

We chose to characterize the strain in the system by micropatterning directional strain gauges on the ferroelectric surface and to characterize the electrical properties of the $MoTe_2$ device using standard transfer curve measurements (Fig. 1a). Dynamic strain from the ferroelectric was measured through strain gauges patterned using the same thin-film Ni as the contact pads to the $MoTe_2$ channel. Therefore, changes in strain in the gauge, as the ferroelectric is poled, represent an experimental measure of changes in the thin-film stress applied to $MoTe_2$ at the contact pads by the contact metal. Strain starts off bipolar with the electric field, as is typical for ferroelectrics, then, on further cycling, develops an asymmetry that causes a transition to unipolar (non-volatile) operation. This asymmetry is independent of the crystal orientation of the ferroelectric and the direction of the gauge. We attribute the asymmetry in the strain curves to the well-known effect of elastic dipoles in ferroelectric systems causing an internal electric-field bias effect[11,12] as they are aligned due to thin-film stress from Ni while the thin film is worked[13] (see discussion in Supplementary Information and Supplementary Fig. 15). Because the size of the strain gauges is large relative to the individual domain structure of the ferroelectric (100 μm versus 1 μm), we see an aggregate strain effect, where individual $MoTe_2$ flakes may feel domain-dependent strain[14].

To test the effect of strain on our devices, we patterned an exfoliated flake of 13 nm 1T′-$MoTe_2$ with 35 nm Ni contact pads, which applied a measured in-plane tensile stress of 0.58 GPa to $MoTe_2$ at the contacts (Supplementary Table 1). The measured transfer characteristics on a linear scale are presented in Fig. 1d, which shows a reversible room-temperature on–off switching behaviour that matches the standard strain butterfly curve in ferroelectric materials (Fig. 1c). We observed substantial changes (>1 order of magnitude) in channel conductivity in more than ten other $MoTe_2$ devices of various thicknesses on various PMN-PT (011) substrates and observed similar bipolar effects. Several devices required multiple sweeps of gate electric field before the strain-driven conductivity changes occurred, but these repeated for several cycles afterwards in a stable state after training. This training behaviour could be a result of enhanced adhesion between the $MoTe_2$ and the ferroelectric upon cycling[15]. Variation in adhesion to rough substrates may contribute to some of the observed differences in training (Supplementary Fig. 12). The bipolar nature of the channel current with respect to the electric field strongly suggests a strain-driven phase transition between the semimetallic and semiconducting phases of $MoTe_2$, where the strain in the $MoTe_2$ flakes evolves with applied gate voltage across the ferroelectric. We note that, in our

[1]Department of Electrical and Computer Engineering, University of Rochester, Rochester, NY, USA. [2]Department of Physics and Astronomy, University of Rochester, Rochester, NY, USA. [3]Electronic Materials Research Laboratory, Key Laboratory of the Ministry of Education and International Center for Dielectric Research, Xi'an Jiaotong University, Xi'an, Shaanxi, China. [4]Department of Mechanical Engineering, University of Rochester, Rochester, NY, USA. *e-mail: stephen.wu@rochester.edu

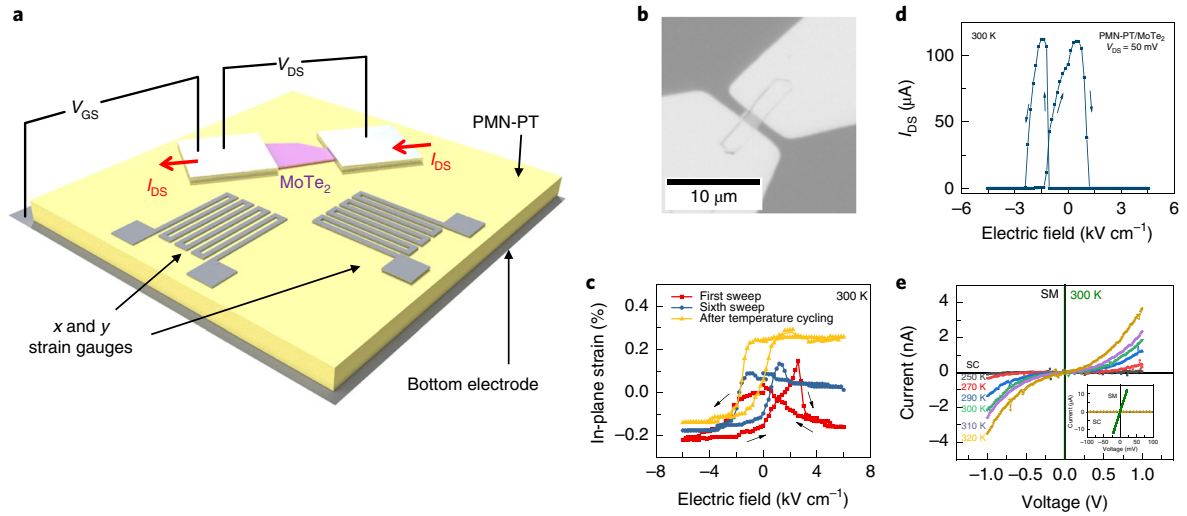

Fig. 1 | Device schematic and operation. a, Schematic representation of the ferroelectric strain field-effect device. **b**, Optical micrograph of actual $MoTe_2$ on the PMN-PT (011) device used in Figs. 2 and 3. **c**, Measured strain curves from as-deposited Ni strain gauges measuring evolution of strain in thin-film Ni contacts, after the 1st sweep, the 6th sweep and finally after temperature cycling to 250 K to 330 K and back to 300 K. **d**, Strain-induced transistor operation on a 13 nm $MoTe_2$ channel, with device $W/L = 2$. **e**, Current–voltage (I–V) characteristics of representative devices in the semimetallic (SM) and semiconducting (SC) states, with the semiconducting state showing Schottky behaviour with respect to temperature. Inset, the same I–V curves on an expanded scale to highlight the semimetallic state.

subsequent testing, $MoTe_2$ flake thickness was not significantly correlated with differences in device behaviour once a phase change had occurred but might still influence whether phase changes can occur at all due to insufficient strain transfer. We chose to focus on devices that had shown clear changes in phase as measured through electrical characterization.

To prove that this behaviour results in a transition to a semiconducting phase, we measured current–voltage characteristics in the low-conductivity state of a representative device of the same geometry and observed a double Schottky junction between the Ni contacts and the phase-transformed $MoTe_2$ channel (Fig. 1e). We note that in our process only 1T′-$MoTe_2$ was used and thus no material with a gap existed within our transistor structure as fabricated; the Schottky-like behaviour only appeared after a transition to the low-conductivity state as a result of strain-driven switching.

To further examine the phase transition in these devices, we performed temperature-dependent measurements of channel conductivity in another $MoTe_2$ device with a nominal thickness of 70 nm, using a PMN-PT (011) substrate with Ni contact electrodes. An optical micrograph of the actual measured device is presented in Fig. 1b. Log-scale conductivity is shown in Fig. 2, showing a unique temperature evolution on sweeping from 300 K to 270 K to 330 K and back to 300 K. Both bipolar and unipolar (non-volatile) channel conductivity modulations were observed, with a maximum $G_{on}/G_{off} \approx 6.2 \times 10^6$ in the final 300 K state, which is a larger value than reported so far for 2H-$MoTe_2$ field-effect transistors using any contact scheme for any thickness[16–18]. For a channel thickness of 70 nm, representing ~100 layers of $MoTe_2$, conventional field-effect conductivity modulation is limited to less than one order of magnitude due to electric field screening in the semiconductor[19]. By purposely choosing a contact metal that exhibits Schottky contact behaviour with semiconducting $MoTe_2$, our ‘off state’ becomes two back-to-back Schottky diodes exhibiting low current when bias voltages are kept low.

Because $MoTe_2$ flakes may land on any single ferroelectric domain within the PMN-PT domain structure, it is understandable why device to device variation may occur as strain directionality may play a large role in seeding the phase transition[14,20]. These uncontrolled factors lead to variation in the bipolar modulation behaviour, with Fig. 2 showing the opposite result of Fig. 1. The unique temperature hysteresis within this device can be understood from the perspective that the phase boundary with respect to strain is highly temperature dependent (Supplementary Fig. 15), which has been measured in the past in 2H-$MoTe_2$, suggesting that the 2H phase is more favourable at low temperatures[21]. As measured through our strain gauges, continued electric field sweeping of the ferroelectric causes the electrical characteristics of our device to transition from bipolar to unipolar operation, as the strain from the Ni contacts changes and eventually reaches a stable unipolar strain after repeated cycling. The majority of device behaviour from Fig. 2 can therefore be explained by noting that the semiconducting phase is more stable at low temperature, while the semimetallic phase is more stable at high temperature, and that the variation in transfer characteristics with electric-field sweeping is due to variation in the strain applied to the $MoTe_2$ from the Ni contacts. There are other uncontrolled factors that may also contribute to a smaller degree, including differential thermal contraction, thin-film stress relaxation with respect to temperature and the temperature dependence of the piezoelectric coefficient in PMN-PT. We note that with further engineering beyond our initial presentation here, it is possible to obtain unipolar or bipolar behaviour by engineering ferroelectric strain from selective electric-field sweeping[22], ferroelastic domain switching[23] or internal electric-field bias engineering[24].

To directly view a real-space image of the channel under ferroelectric strain, we used conductive atomic force microscopy (CAFM) to directly probe the channel conductivity. Figure 3 shows the results of CAFM scans of the device presented in Fig. 2 directly after measurement (left in the low conductivity state) with both contact pads grounded with respect to the voltage-biased CAFM tip. A large non-conductive area is located near the contact edge of the device, representing the semiconducting phase of $MoTe_2$ and hinting at effects arising from contact-metal-induced strain. We further examined the effect of strain on this channel by applying a gate voltage pulse to set the conductivity state of the channel, as schematically represented by the hysteresis loops in Fig. 3c–e. As a control measurement, we first pulsed the gate in the direction in which the device was already set; Fig. 3d shows that the large non-conducting region at the contact edge is retained, but is now also mirrored at

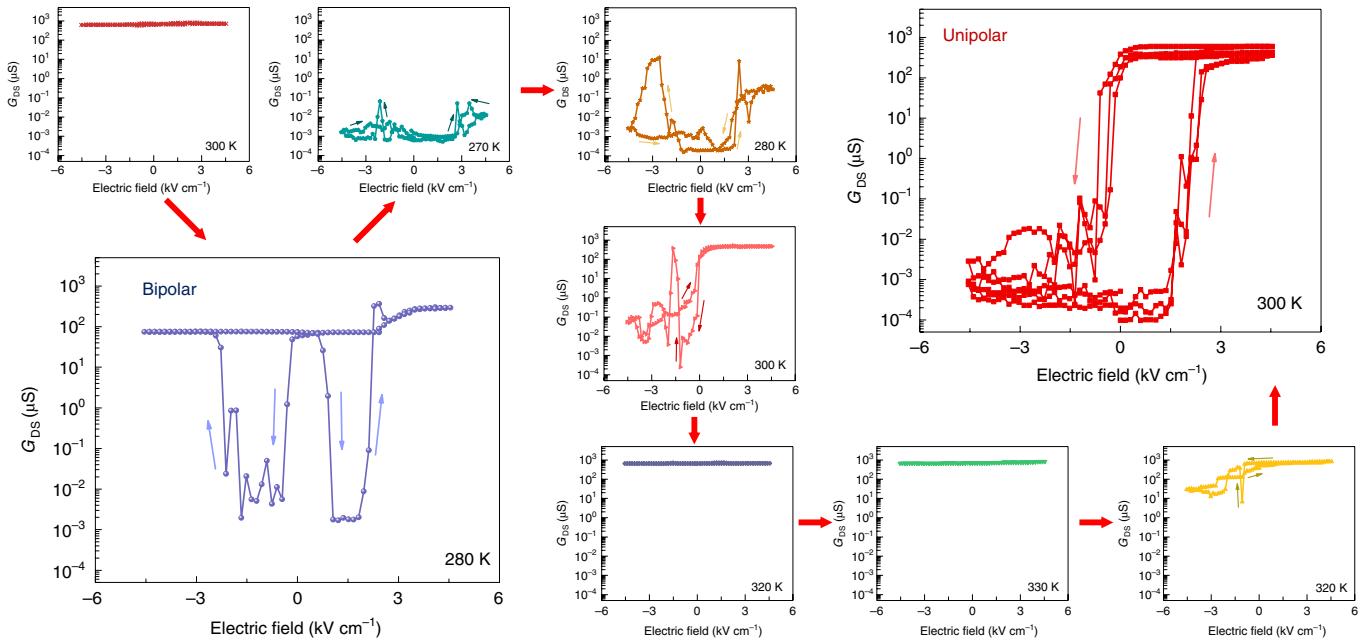

Fig. 2 | Temperature cycling and non-volatile switching. Log-scale channel conductance measurements for the device presented in Fig. 1b (70 nm channel, $W/L = 2.3$) with respect to temperature cycling, starting at 300 K then 270 K to 330 K to 300 K. Measurements are taken with $V_{ds} = 100$ mV and are current-limited at 100 μA. Transitions between the full semimetallic state and Schottky-barrier-limited operation in the semiconducting state are shown. Depending on temperature history, large variations in device behaviour exist due to strain evolution and the temperature dependence of the phase transition. Both bipolar and unipolar (non-volatile) behaviours are seen in the devices. The final unipolar device at a single temperature is robust, as shown by three full major loop sweeps. Additional data on temperature dependence, unipolar behaviour and device stability are provided in the Supplementary Information (Supplementary Figs. 3 and 5).

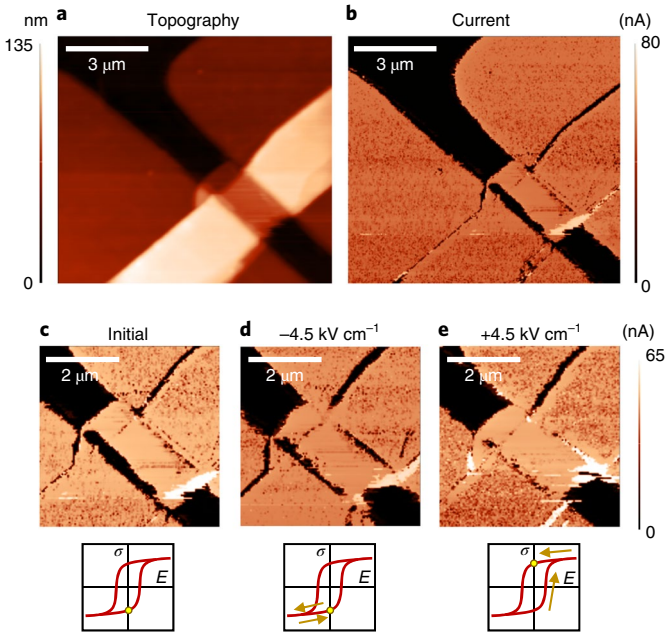

Fig. 3 | Conductive atomic force microscopy of switching behaviour. **a**,**b**, Topography and current, measured by CAFM, of the device presented in Fig. 2 after being left in the low conductivity state (290 K). Large changes in conductivity can be inferred from CAFM data near the contact edges. **c**–**e**, CAFM images after a pulse sequence representing the initial condition (**c**), then a pulse in the same direction as polarization (**d**) and finally a pulse in the opposite direction as polarization (**e**). Channel near the contact edges retains low conductivity in **d**, while the edges show higher conductivity after the opposite pulse (**e**).

the other contact edge. The initial asymmetry of the CAFM image (Fig. 3c) is due to the gate voltage being applied with respect to the source contact (from the measurement in Fig. 2), whereas the first and second pulses (Fig. 3d,e) are applied with respect to both source and drain. Next a pulse was applied in the positive direction to switch the channel to the conducting state; Fig. 3e shows that the non-conductive regions near the contacts are now closed. This suggests that the strain-driven phase transition is seeded by strain from the thin-film stress induced by the contacts.

We explored the effect of substrate crystal orientation and further examined the effect of contact metals on the behaviour of our devices by investigating more $MoTe_2$ devices on PMN-PT (111) substrates. Figure 4a shows the same current map measured using CAFM on a $MoTe_2$/PMN-PT (111) device with the same Ni contacts, showing the same characteristic phase change behaviour at the contact edges but on a device with a shorter channel. Our contact strain hypothesis is supported by a finite-element analysis simulation of the strain state within a $MoTe_2$ channel given tensile strain from the edges, which shows the same characteristic shape as the current map. Further modelling performed on a longer channel device, similar to the device presented in Fig. 3, shows the same correspondence (Supplementary Fig. 6). With the calculated strain induced into the $MoTe_2$ channel from contact-induced stress (using literature values for the Young's modulus and Poisson's ratio of $MoTe_2$; ref. [21]) and the characteristic size of the semiconducting region as measured by CAFM at the contact edge, we can extract the approximate threshold for the phase transition. We find that the contacts apply tensile strain to the $MoTe_2$ at 0.4%, and the strain threshold occurs at ~0.33% based on the length scale that the semiconducting region bleeds out at the Ni contacts on the device from Fig. 3. The magnitude of this strain is comparable to both experimentally observed and theoretically predicted strain transitions in $MoTe_2$ (refs. [20,21,25]), as well as the amount of electric-field-controllable

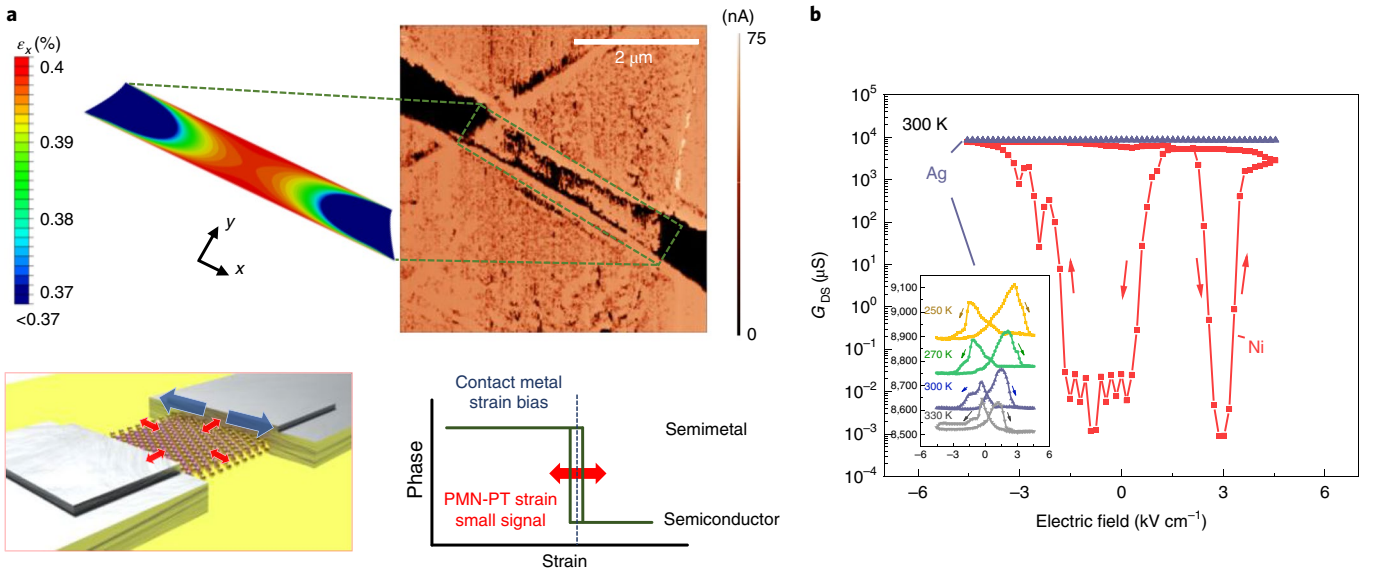

Fig. 4 | Effect of contact metals and simulations. a, CAFM image of a 50 nm $MoTe_2$ device ($W/L = 6.3$) patterned with Ni contacts on a PMN-PT(111)-oriented single crystal showing contact edge effects. The data are shown with a finite-element analysis simulation of strain in the channel assuming clamped tensile strain from the contact metal. The device operation, based on contact metal-induced strain, is presented below, where electric-field-controllable strain from PMN-PT (red) is used to modulate over contact-induced strain (blue). The proposed mechanism of operation of a strain-biased PMN-PT device is also presented. **b**, Channel conductance on $MoTe_2$ devices with Ag (low compressive stress, −0.2 GPa) and Ni (larger tensile stress, 0.58 GPa) contacts. Only a small modulation in conductivity is seen in Ag contact devices (~4%) versus Ni devices (~10^9%). Inset, temperature evolution of an Ag contact device.

strain in PMN-PT as measured in Fig. 1c. Because these devices were patterned on PMN-PT (111), this suggests that the phase transitions are robust against ferroelectric orientation. We expect that these microscale devices do not depend heavily on the overall aggregate strain behaviour of the ferroelectric single crystal, but on the individual ferroelectric domains on which the $MoTe_2$ channel and contacts land[14].

Using different contact metals on PMN-PT(111), we also showed that phase transitions are only robust when contact metals apply a finite tensile stress (Ni). Unlike low-stress contacts (−0.2 GPa) made of 50 nm Ag, where conductivity changes are limited to the few percent range at all temperatures, a similar Ni device demonstrates conductivity changes of ~10^9% (Fig. 4b). Of 13 measured devices with Ag contacts on both PMN-PT(011)- and (111)-oriented substrates, none showed any meaningful conductivity modulation other than a marginal few percent change. To further prove the necessity of a tensile stressor layer, an alternative $MoTe_2$ device was also constructed with low-stress Ag contacts encapsulated in a high-stress tensile insulating MgF_2 layer as the static stressor. With MgF_2 applying a similar-magnitude tensile strain as Ni (Supplementary Fig. 10), the devices again returned to large conductivity switching with PMN-PT (Supplementary Fig. 11).

The overall predicted mechanism of operation based on our experimental devices is outlined in Fig. 4a. Thin-film stress from contact metal deposition sets a higher strain state than a single ferroelectric can apply by itself, while a small amount of electric-field-controllable strain from PMN-PT can bring the $MoTe_2$ across the phase boundary. This suggests that the majority of the channel conductivity changes happen underneath the contacts, and our CAFM measurements are only able to incidentally observe phase transitions at the edges in special cases. This is supported by the fact that no CAFM measurement on any device showed channel conductivity changes further than 250–500 nm away from the contact edges. The use of 1T′-$MoTe_2$ as the starting material allows the two contact sides to always be connected through a metallic link, such that large changes that occur near the contacts are reflected in the final electrical measurement. Phase transitions were not observed when using 2H-$MoTe_2$ as the starting material with Ni contacts, although presumably through thin-film strain engineering it can become possible in a different geometry. We also note that while the majority of the devices showed large changes in conductivity, approximately 8 out of 28 measured devices on both (011) and (111) PMN-PT using Ni contacts also had low modulation in the few percent range (1/3 on (111) and 1/4 on (011)) (Supplementary Fig. 7). We attribute this variation to the various uncontrolled aspects of our devices: whether each $MoTe_2$ flake lands on single or multiple ferroelectric domains, what the polarization of the domain is (setting the zero strain starting state)[14], which direction the ferroelectric strain exists in with respect to the contact metal, and what the crystal orientation of the $MoTe_2$ was when exfoliated.

To further examine the properties of the semiconducting region in our devices after phase changes had occurred, we performed backside Raman spectroscopy on $MoTe_2$ devices with Ni contacts fabricated on transparent double-side-polished MgO substrates (0.25 mm thickness) in the same geometry as on PMN-PT substrates (Supplementary Figs. 13 and 14). By performing Raman measurements through the substrate, we were able to examine the phase-changed material underneath the Ni contact. We found that the semiconducting phase in our $MoTe_2$ devices is not the 2H semiconducting phase, and the additional Raman peaks that appear are similar to Raman signatures from other phase-transformed $MoTe_2$ devices from the literature (driven by strain[21] or laser heating[16]). Detailed discussions about the exact nature of the structural-phase change in our devices, as well as a thorough elimination of potential trivial non-strain-induced phase-change mechanisms, are provided in the Supplementary Information.

We endurance-tested Ni contact devices and observed that reliable and stable switching behaviour only occurred for between 40 and 70 switches (Supplementary Fig. 4). Beyond this, the device became unstable as a result of the transfer characteristics changing

upon further device cycling. A potential source of instability is the thickness of our samples, as strain cannot be fully transferred without eventual slippage between van der Waals bonded layers. Recent studies have shown that strain can be applied in two-dimensional (2D) bonded systems up to 40 nm (ref. [26]), although the exact nature of strain transfer from the 3D bonded limit to the 2D bonded limit needs to be further explored before the exact nature of interlayer slippage can be quantified[27,28]. For the eventual application of a strain transistor, reducing the device thickness to the monolayer limit will become important to eliminate the variable of layer sliding to further explore other device failure mechanisms and to find the ultimate limit of endurance in our strain-driven devices. Other factors in endurance may include effects such as improper flake adhesion or plastic deformation of static stressor layers. Devices have also been tested for speed and have been shown to switch with gate voltage pulses of 10 ms. This is the limit of our experimental capability as we switched the entire single-crystal ferroelectric over 0.25–0.3 mm, which requires pulses of 150 V. Further testing on thin-film ferroelectrics will need to be performed to find the true limit for the speed of strain switching. The ultimate limit is probably similar to existing speeds of $MoTe_2$ phase change memristors that operate down to the nanosecond scale[29], with the potential to go as low as the picosecond range because ferroelectric switching has been shown to operate in this range[6]. Finally, while PMN-PT and $MoTe_2$ are used in this first demonstration, many other materials have been proposed to be sensitive to strain-based phase change[20,30], and many different ferroelectrics[6] can be used to further engineer strain. Further development of materials for electrical and mechanical properties will become important to engineer for the factors listed above as development becomes more important for this technology.

We have introduced a new type of transistor where electric-field-induced strain can reversibly change the device between semimetallic and semiconducting. Strain-induced phase changes do not suffer from the same limitations as conventional field-effect transistors in terms of obtaining large on–off ratios while retaining fast switching outside of subthreshold slope limitations. The 'on' state of our device is fully metallic, leading to exceptionally high 'on' currents, while the 'off' state can be engineered for small current leakage through contact engineering. As the devices do not heavily depend on the thickness of the $MoTe_2$ channel and retain the three-terminal gate configuration from conventional field-effect transistors, the process to scale these devices into realistic commercial integrated circuits becomes significantly less challenging. This type of 'straintronic' device combines the best properties of 2D materials (large elastic limit, immunity to strain-induced breakage, wide variety of phases) with the best properties of ferroelectrics (low-power, non-volatile, fast switching). The performance of the individual constituent elements suggests that there is a much higher ceiling to device performance than presented here in our first demonstration. Looking beyond $MoTe_2$, using strain-engineered 2D materials with ferroelectrics represents a fundamentally exciting platform to explore the wide variety of other electric-field-induced phase transitions in the 2D materials world (that is, magnetic[31], topological[32], superconducting[33] and so on), leading to a new method for low-power control over various quantum and conventional states of matter.

Online content

Any methods, additional references, Nature Research reporting summaries, source data, statements of code and data availability and associated accession codes are available at https://doi.org/10.1038/s41565-019-0466-2.

Received: 26 May 2018; Accepted: 26 April 2019;
Published online: 10 June 2019

References

1. Zhirnov, V. V. & Cavin, R. K. Nanoelectronics: negative capacitance to the rescue? *Nat. Nanotechnol.* **3**, 77–78 (2008).
2. Cheung, K. P. On the 60 mV/dec @300 K limit for MOSFET subthreshold swing. In *Proceedings of 2010 International Symposium on VLSI Technology, System and Application* 72–73 (IEEE, 2010).
3. Frank, D. J. et al. Device scaling limits of Si MOSFETs and their application dependencies. *Proc. IEEE* **89**, 259–288 (2001).
4. Pimbley, J. M. & Meindl, J. D. MOSFET scaling limits determined by subthreshold conduction. *IEEE Trans. Electron Devices* **36**, 1711–1721 (1989).
5. Muller, J., Polakowski, P., Mueller, S. & Mikolajick, T. Ferroelectric hafnium oxide based materials and devices: assessment of current status and future prospects. *ECS J. Solid State Sci. Technol.* **4**, N30–N35 (2015).
6. Hong, X. Emerging ferroelectric transistors with nanoscale channel materials: the possibilities, the limitations. *J. Phys. Condens. Matter* **28**, 103003 (2016).
7. Manipatruni, S. et al. Scalable energy-efficient magnetoelectric spin–orbit logic. *Nature* **565**, 35–42 (2019).
8. Chen, A. A review of emerging non-volatile memory (NVM) technologies and applications. *Solid State Electron.* **125**, 25–38 (2016).
9. Lee, M. L., Fitzgerald, E. A., Bulsara, M. T., Currie, M. T. & Lochtefeld, A. Strained Si, SiGe and Ge channels for high-mobility metal-oxide-semiconductor field-effect transistors. *J. Appl. Phys.* **97**, 011101 (2005).
10. Okino, H., Sakamoto, J. & Yamamoto, T. Cooling-rate-dependence of dielectric constant and domain structures in $(1-x)Pb(Mg_{1/3}Nb_{2/3})O_3$–$xPbTiO_3$ single crystals. *Jpn J. Appl. Phys.* **44**, 7160–7164 (2005).
11. Genenko, Y. A., Glaum, J. & Hoffmann, M. J. Mechanisms of aging and fatigue in ferroelectrics. *Mater. Sci. Eng. B* **192**, 52–82 (2015).
12. Arlt, G. & Neumann, H. Internal bias in ferroelectric ceramics: origin and time dependence. *Ferroelectrics* **87**, 109–120 (1988).
13. Damodaran, A. R., Breckenfeld, E., Chen, Z., Lee, S. & Martin, L. W. Enhancement of ferroelectric Curie temperature in $BaTiO_3$ films via strain-induced defect dipole alignment. *Adv. Mater.* **26**, 6341–6347 (2014).
14. Buzzi, M. et al. Single domain spin manipulation by electric fields in strain coupled artificial multiferroic nanostructures. *Phys. Rev. Lett.* **111**, 027204 (2013).
15. Du, H., Xue, T., Xu, C., Kang, Y. & Dou, W. Improvement of mechanical properties of graphene/substrate interface via regulation of initial strain through cyclic loading. *Opt. Lasers Eng.* **110**, 356–363 (2018).
16. Cho, S. et al. Phase patterning for ohmic homojunction contact in $MoTe_2$. *Science* **349**, 625–628 (2015).
17. Lin, Y.-F. et al. Ambipolar $MoTe_2$ transistors and their applications in logic circuits. *Adv. Mater.* **26**, 3263–3269 (2014).
18. Qu, D. et al. Carrier-type modulation and mobility improvement of thin $MoTe_2$. *Adv. Mater.* **29**, 1606433 (2017).
19. Fathipour, S. et al. Exfoliated multilayer $MoTe_2$ field-effect transistors. *Appl. Phys. Lett.* **105**, 192101 (2014).
20. Duerloo, K.-A. N., Li, Y., Reed, E. J., Scuseria, G. E. & Heinz, T. F. Structural phase transitions in two-dimensional Mo- and W-dichalcogenide monolayers. *Nat. Commun.* **5**, 4214 (2014).
21. Song, S. et al. Room temperature semiconductor-metal transition of $MoTe_2$ thin films engineered by strain. *Nano Lett.* **16**, 188–193 (2016).
22. Wu, T. et al. Domain engineered switchable strain states in ferroelectric (011) $[Pb(Mg_{1/3}Nb_{2/3})O_3]_{(1-x)}$-$[PbTiO_3]_x$ (PMN-PT, $x \approx 0.32$) single crystals. *J. Appl. Phys.* **109**, 124101 (2011).
23. Yang, L. et al. Bipolar loop-like non-volatile strain in the (001)-oriented $Pb(Mg_{1/3}Nb_{2/3})O_3$-$PbTiO_3$ single crystals. *Sci. Rep.* **4**, 4591 (2015).
24. Pesic, M. et al. Built-in bias generation in anti-ferroelectric stacks: methods and device applications. *IEEE J. Electron. Devices Soc.* **6**, 1019–1025 (2018).
25. Li, X., Wu, M., Xu, B., Liu, R. & Ouyang, C. Compressive strain induced dynamical stability of monolayer 1T-MX_2 (M = Mo, W; X = S, Se). *Mater. Res. Express* **4**, 115018 (2017).
26. Vermeulen, P. A., Mulder, J., Momand, J. & Kooi, B. J. Strain engineering of van der Waals heterostructures. *Nanoscale* **10**, 1474–1480 (2018).
27. Wang, R. et al. 2D or not 2D: strain tuning in weakly coupled heterostructures. *Adv. Funct. Mater.* **28**, 1705901 (2018).
28. Kumar, H., Dong, L. & Shenoy, V. B. Limits of coherency and strain transfer in flexible 2D van der Waals heterostructures: formation of strain solitons and interlayer debonding. *Sci. Rep.* **6**, 21516 (2016).
29. Zhang, F. et al. Electric-field induced structural transition in vertical $MoTe_2$- and $Mo_{1-x}W_xTe_2$-based resistive memories. *Nat. Mater.* **18**, 55–61 (2019).
30. Kalikka, J. et al. Strain-engineered diffusive atomic switching in two-dimensional crystals. *Nat. Commun.* **7**, 11983 (2016).
31. Manchanda, P., Sharma, V., Yu, H., Sellmyer, D. J. & Skomski, R. Magnetism of Ta dichalcogenide monolayers tuned by strain and hydrogenation. *Appl. Phys. Lett.* **107**, 032402 (2015).
32. Xiang, H. et al. Quantum spin Hall insulator phase in monolayer WTe_2 by uniaxial strain. *AIP Adv.* **6**, 095005 (2016).
33. Ge, Y., Wan, W., Yang, F. & Yao, Y. The strain effect on superconductivity in phosphorene: a first-principles prediction. *New J. Phys.* **17**, 035008 (2015).

Acknowledgements

This work made use of the Cornell Center for Materials Research Shared Facilities, which are supported through the NSF MRSEC programme (DMR-1719875). The authors thank D.H. Kelley for the borrowed usage of his MBraun glovebox, as well as A. Nick Vamivakas and A. Mukherjee for discussions and assistance with micro-Raman spectroscopy.

Author contributions

Device fabrication was performed by W.H., A.S., T.P. and A.A. Device characterization was performed by W.H., A.A. and S.M.W. CAFM was performed by W.H., A.S. and S.M.W. Strain gauge calibration was performed by W.H. and S.M.W. Topographic AFM and optical contrast calibration was performed by T.P. Thin-film stress measurements were performed by C.W., A.A., W.H. and S.M.W. Piezoresponse force microscopy was performed by C.W. Raman spectroscopy was performed by A.A. and S.M.W. Finite-element analysis simulation was performed by H.A. PMN-PT single crystals were provided by M.L. The original experiment conception and project supervision were provided by S.M.W.

Competing interests

The authors declare no competing interests.

Additional information

Supplementary information is available for this paper at https://doi.org/10.1038/s41565-019-0466-2.

Reprints and permissions information is available at www.nature.com/reprints.

Correspondence and requests for materials should be addressed to S.M.W.

Journal peer review information: *Nature Nanotechnology* thanks Young Hee Lee and Robert Simpson for their contribution to the peer review of this work.

Publisher's note: Springer Nature remains neutral with regard to jurisdictional claims in published maps and institutional affiliations.

Methods

Device fabrication. The devices were fabricated on PMN-PT single crystals (0.25–0.3 mm thickness) with sputtered Au (100 nm)/Ti (5 nm) bottom electrode contacts. Commercially purchased 1T′-$MoTe_2$ (HQ Graphene) was exfoliated onto the polished ($R_a \approx 0.5$ nm) side of the PMN-PT using standard Nitto Semiconductor Wafer Tape SWT10. Exfoliation was performed in a low-humidity room (relative humidity, <10%) or in a controlled glovebox with <1 ppm of H_2O and O_2. Optical contrast thickness identification was used to characterize the thickness of the flakes (Supplementary Figs. 8 and 9), which are then reconfirmed with atomic force microscopy. Direct-write laser photolithography was performed using a Microtech LW405 laserwriter system, with S1805 photoresist specifically softbaked at low temperatures (80 °C) to prevent heating above the Curie temperature. If standard bake recipes for photoresists and electron-beam resists are used, spontaneous quenching through the Curie temperature will occur and result in devices that do not produce larger than a few percent conductance modulation. Patterns were exposed using standard photolithographic doses of 300 mJ cm^{-2}, and the photoresist was soaked in chlorobenzene for 5 min before development for undercut control. All contact metals were deposited using electron-beam evaporation at 5×10^{-5} torr at a rate of 1 Å s^{-1}. Strain gauges were constructed from the same thin-film deposition (35 nm Ni) and separately calibrated using flexible Kapton substrates with strain applied by bending. The axial and transverse gauge factors were measured to be 3.1 and 0.15, respectively, limiting the contributions of strain perpendicular to the axial direction by a factor of over 20.

Device characterization. The devices were characterized using low-frequency a.c. lock-in techniques (3 Hz) with the a.c. voltage signal provided by a separate phase-locked function generator. Conductivity measurements were performed with an applied voltage of 100 mV and a 100 µA current-limiting circuit to prevent device blowout because the high conductivity states are purely metallic and large current densities can form when the phase transition occurs. More detailed measurements of Ag electrode devices were performed with 10 mV applied voltage with the same current limiter, but all devices were first tested under the same conditions as Ni electrode devices to confirm the null result. Gate voltages were applied between the backgate and the source contact in the device using a d.c. power supply and were typically applied for 5 s before each conductivity measurement. All devices were swept in the positive electric field direction first and cooled in negative remanence when temperature cycling unless otherwise noted.

CAFM. Devices were measured using conductive tips coated using confocal d.c. sputtering of 10 nm W, followed by 20 nm Pt. Measurements were performed in contact mode, with the force setpoint low to prevent sample damage during scanning. Pulse measurements were carried out by removing the device from the AFM, ramping the voltage on the gate relative to both grounded contact pads over 30 s, and then ramping down to 0 V. Devices were then placed back into the AFM for the next CAFM measurement.

Finite-element analysis. Finite-element analysis was performed using the Abaqus FEA software suite. A membrane with the same dimensions as the thin film was modelled with quadratic plane elements with an average side length of 0.05 µm. A lateral strain of 0.4% was applied to the contact edges to model the Ni interface strains. The side edges were free. The material was assumed to be isotropic, averaging the anisotropic mechanical properties. Colour coding of the resulting strain contours was set to show the range where switching was expected based on the strain analysis described in the main text.

Raman spectroscopy. Raman spectroscopy was performed using a Renishaw InVia Confocal Raman Microscope, with a ×50 long working distance objective to image through the transparent double-side-polished ($R_a \approx 0.5$ nm) MgO substrate (532 nm excitation laser). Laser power was limited to 2 mW to limit changes to the device due to heating. Devices were electrically confirmed to be in the semiconducting state using Schottky barrier I–V measurements, then located in the Raman microscope through the backside to gain access to the $MoTe_2$ under the contacts. The estimated spot size of the laser was 1.5 µm.

Data availability

The data that support the findings of this study are available from the corresponding author upon reasonable request.